

# Numerical investigation of the possibility of macroscopic turbulence in porous media: a direct numerical simulation study

Y. Jin<sup>1</sup>, M.-F. Uth<sup>1</sup>, A. V. Kuznetsov<sup>2</sup> and H. Herwig<sup>1,†</sup>

<sup>1</sup>Institute of Thermo-Fluid Dynamics, Hamburg University of Technology, Hamburg, D-21073, Germany

<sup>2</sup>Department of Mechanical and Aerospace Engineering, North Carolina State University, Raleigh, NC 27695-7910, USA

(Received 26 August 2014; revised 28 October 2014; accepted 5 January 2015;  
first published online 2 February 2015)

When a turbulent flow in a porous medium is determined numerically, the crucial question is whether turbulence models should account only for turbulent structures restricted in size to the pore scale or whether the size of turbulent structures could exceed the pore scale. The latter would mean the existence of macroscopic turbulence in porous media, when turbulent eddies exceed the pore size. In order to determine the real size of turbulent structures in a porous medium, we simulated the turbulent flow by direct numerical simulation (DNS) calculations, thus avoiding turbulence modelling of any kind. With this study, which for the first time uses DNS calculations, we provide benchmark data for turbulent flow in porous media. Since perfect DNS calculations require the resolution of scales down to the Kolmogorov scale, often only approximate DNS solutions can be obtained, especially for high Reynolds numbers. This is accounted for by using and comparing two different DNS approaches, a finite volume method (FVM) with grid refinement towards the wall and a lattice Boltzmann method (LBM) with equal grid distribution. The solid matrix was simulated by a large number of rectangular bars arranged periodically. The number of bars in the solution domain with periodic boundary conditions was reduced systematically until a minimum size was found that does not suppress any large-scale turbulent structures. Two-point correlations, integral length scales and energy spectra were determined in order to answer the question of whether or not macroscopic turbulence can be found in porous media.

**Key words:** porous media, turbulence simulation, turbulent convection

---

## 1. Introduction

A flow in a porous medium is characterized by length scales of different magnitudes. Assuming continuous fluid flow, i.e. a sufficiently small Knudsen number, the smallest relevant geometric scale is the pore scale, which can be estimated by the average hydraulic diameter of the pores. Next in the hierarchy of scales comes the size of a representative elementary volume (REV), which is relevant in cases where pores are

† Email address for correspondence: [h.herwig@tuhh.de](mailto:h.herwig@tuhh.de)

of very different individual sizes. For a homogeneous matrix with pores of the same size and a flow in the laminar regime the size of an REV is of the order of the pore size.

These considerations are important when it comes to the question of turbulent flow in porous media. For high enough pore-scale Reynolds numbers the flow within the pores will be turbulent since the connected pores can be viewed as microchannels. Indeed, if the Reynolds number exceeds the critical Reynolds number for such microchannels, the flow becomes turbulent. This is the same as for macroscopic flows through conduits (Wibel & Ehrhard 2006, 2009).

The topic of turbulence in porous media was reviewed in recent books by de Lemos (2012) and Nield & Bejan (2013) and in many review chapters, such as Lage, de Lemos & Nield (2002), de Lemos (2004, 2005), and Vafai *et al.* (2006). There are two distinct views on turbulence in porous media. The first view was originally expressed in Nield (1991, p. 271) and then further developed in Nield (2001). According to this view, true macroscopic turbulence, at least in a dense porous medium, is impossible because of the limitation on the size of turbulent eddies imposed by the pore scale. This prevents the transfer of energy from large to smaller turbulent eddies. Thus, any turbulence in porous media is restricted to turbulence within the pores.

Although most published turbulence models attempt to obtain macroscopic characteristics of flow in porous media, some of them do this by simulating pore-scale turbulence. According to Nield (2001), the model developed by Nakayama & Kuwahara (1999), due to the size of the periodic cell and the assumption of periodicity, in fact simulates turbulence within the pores. The same applies to Kuwahara *et al.* (1998).

The second class of models deals primarily with macroscopic turbulence in porous media. Representative models are those developed by Lee & Howell (1991), Prescott & Incropera (1995) and Antohe & Lage (1997). Macroscopic turbulence models have also been used to simulate flow in a porous matrix represented by a periodic array of square cylinders (Kazerooni & Hannani 2009; Kundu, Kumar & Mishra 2014).

Finally, many turbulence models attempt to simulate both pore-scale turbulence and large-scale turbulence. Representative models are those developed by de Lemos and colleagues, see de Lemos & Pedras (2000, 2001), Pedras & de Lemos (2000, 2001a,b,c, 2003), Rocamora & de Lemos (2000), de Lemos & Rocamora (2002), de Lemos & Braga (2003), de Lemos & Mesquita (2003), Silva & de Lemos (2003) and de Lemos & Tofaneli (2004).

The crucial question about the presence of macroscopic turbulence in porous media cannot be addressed by Reynolds-averaged Navier–Stokes (RANS) equations and not even by large-eddy simulation (LES), since these approaches involve turbulence modelling which implicitly or explicitly involves presupposition about the size of turbulent eddies. The only way to answer this question without ambiguity is to refer to experiments or to direct numerical simulation (DNS) solutions, which resolve turbulent flow accounting for all scales down to the Kolmogorov scale. Since measurements within the porous matrix are more than challenging, DNS solutions appear to be the best alternative.

In this paper we present results of extensive DNS investigations of the flow through a generic porous matrix (GPM) described and discussed in § 2.

## 2. The porous matrix

### 2.1. The REV for turbulent flow

In order to define an REV we need to determine the smallest subvolume of a porous matrix that shows the same flow behaviour as the flow behaviour that exists in the

whole matrix. In the introduction it was argued that the REV is of the order of the pore size when the flow is laminar (a low Reynolds number) and the matrix is geometrically regular on the pore size. We called this REV-L and in addition introduced a representative elementary volume REV-T. The REV-T is for a turbulent flow; it must be larger than the REV-L if macroscopic turbulent eddies exist with sizes much larger than the pore size.

By carefully selecting the size of REV-T, we avoid possible suppression of large-scale turbulence caused by the periodicity of our model. This limitation is discussed in Nield (2001), who pointed out that by simulating flow in a periodic cell one may *a priori* rule out global eddies. We avoided this problem by making our REV-T sufficiently large.

The main questions (assuming a regular porous matrix) are as follows.

- (i) What is the size of REV-T?
- (ii) Is REV-T much larger than REV-L in size, i.e. are there macroscopic turbulent eddies in porous media?

## 2.2. A GPM for a DNS analysis

In order to investigate the size of turbulent eddies in porous media, we designed a GPM. We used the following three assumptions.

- (i) The matrix may have a regular structure since the size of turbulent eddies will not be affected too much by irregularity of the matrix.
- (ii) The matrix may be geometrically two-dimensional. This is because the turbulent flow will be three-dimensional anyway, irrespective of whether the solid matrix is two- or three-dimensional.
- (iii) The porosity in our model is taken to be relatively high (0.78–0.94), since smaller porosity will only result in stronger suppression of any possible macroscopic turbulence. Thus, by selecting a porous matrix with a high porosity we are not risking the suppression of any macroscopic turbulence that might occur otherwise, i.e. for low porosity.

Figure 1 shows our GPM built from a large number of rectangular bars that were arranged periodically to form a porous medium. For this geometry, the porosity  $\varphi$  is defined as

$$\varphi = 1 - \frac{1}{2} \left( \frac{d}{s} \right)^2, \quad (2.1)$$

where  $s$  is the pore size and  $d$  is the elementary bar size (see figure 1). The permeability of the GPM can be evaluated using correlations presented in Dullien (1992). For our GPM, a larger porosity corresponds to a larger permeability. Since the permeability can be expressed in terms of geometrical parameters of the porous matrix, in our analysis we only specify the pore size and porosity.

Within this regular geometric structure a representative volume REV-L is of size  $2s$  while the size of REV-T is yet unknown. A strategy to find the REV-T size was as follows. We started with an REV-T that included a large number of elementary bars, calculated the turbulent flow in that domain and then reduced the number of bars systematically. As long as the results in a smaller domain were the same as the corresponding results in a larger domain, a further reduction was appropriate.

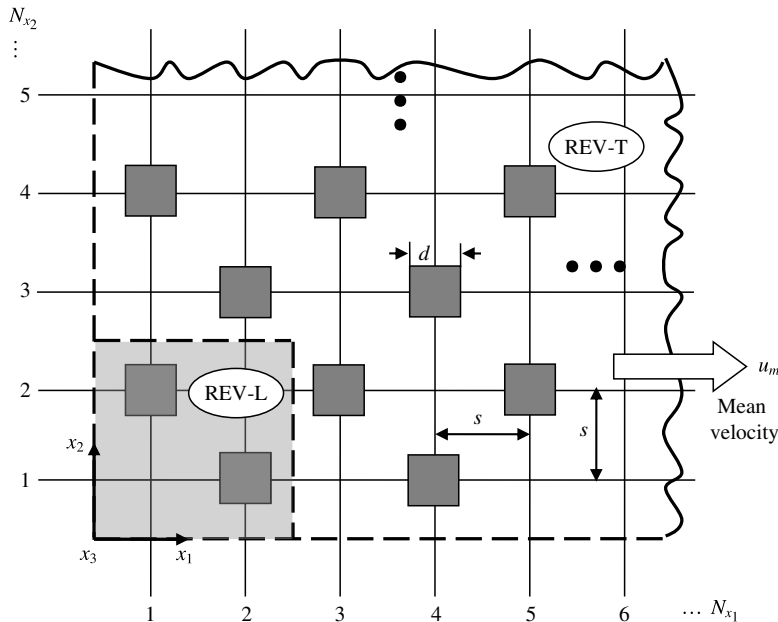


FIGURE 1. The GPM with the representative elementary volumes REV-L and REV-T (REV-T occupies the whole area shown in figure 1). Here, ' $u_m$ ' is the mean flow velocity, ' $N_{x_1}$ ' is the size of the REV-T in the ' $x_1$ ' direction (in pore sizes), and ' $N_{x_2}$ ' is the size of the REV-T in the ' $x_2$ ' direction.

### 3. Direct numerical simulation calculations in a porous medium

#### 3.1. Preliminary remarks

The only way to completely avoid turbulence modelling in computational fluid dynamics (CFD) solutions is to directly simulate the fluid flow, accounting for all relevant length and time scales. This approach is known as DNS; see Moin & Mahesh (1998) for a general introduction. Due to the enormous computational resources required (cpu time and storage capacity), only certain benchmark cases (see Ma, Karamanos & Karniadakis (2000), Parnaudeau *et al.* (2008) and Afgan *et al.* (2011)) or special fundamental problems (Kis 2011; Jin & Herwig 2013, 2014) can be handled by this method.

#### 3.2. Direct numerical simulation methods

Two different methods which complement and verify each other were applied in this study to look for possible macroscopic turbulence in porous media. They are

- (i) an FVM which directly solves the Navier–Stokes equations;
- (ii) an LBM which determines the particle distribution; this method indirectly corresponds to solving the Navier–Stokes equations.

Both methods have been tested against each other in Jin, Uth & Herwig (2015) for the problem of a turbulent flow along a rough wall. In Jin *et al.* (2015) wall roughness was simulated by positioning two-dimensional bars on an otherwise smooth wall, creating a geometry that is similar to the porous medium design shown in figure 1.

##### 3.2.1. The FVM

The governing equations to be solved for an incompressible flow of a Newtonian fluid with an FVM are the Navier–Stokes equations. We non-dimensionalized these

equations with  $d$  and  $u_m$  and used the Einstein summation convention. In Cartesian coordinates these equations read (Herwig 2002)

$$\frac{\partial u_i}{\partial x_i} = 0, \quad (3.1)$$

$$\frac{\partial u_i}{\partial t} + \frac{\partial(u_i u_j)}{\partial x_j} = -\frac{\partial p}{\partial x_i} + \frac{1}{Re} \frac{\partial^2 u_i}{\partial x_j^2} + g_i. \quad (3.2)$$

The Reynolds number in (3.2) is defined as

$$Re = \frac{u_m d}{\nu}, \quad (3.3)$$

where  $u_m$  and  $d$  are defined in figure 1 and  $\nu$  is the kinematic viscosity of the fluid.

Equations (3.1)–(3.3) were solved in a three-dimensional computational domain, the cross-section of which is the REV-T (see figure 1), and which extends in the third direction by a length  $L_3$ , see the discussion of this in § 4.3. We used periodic boundary conditions on all boundaries of our computational domain since REV-T is an arbitrary cutout with respect to the whole porous matrix. By periodic boundary conditions we mean that all flow quantities (except the pressure in the flow direction) are equal on opposing boundaries of the REV-T.

In (3.2)  $g_i$  is a prescribed pressure gradient which ensures a particular flow rate. The solution of (3.1)–(3.3) was advanced in time with the second-order implicit backward Euler method. To compute the derivatives of the velocity, the variables at the interfaces of the grid cells were obtained with linear interpolation. A second-order central difference scheme was used for spatial discretization. The pressure at the new time level was determined by the Poisson equation. The velocity was corrected by the pressure-implicit scheme with splitting of operators (PISO) pressure–velocity coupling.

### 3.2.2. The LBM

This method statistically models the propagation and interaction of particles and thus simulates the flow. For small Mach numbers, the macroscopic velocities that then emerge are solutions of the Navier–Stokes equations.

The basic equation for the LBM is a discretized version of the Boltzmann equation for the particle distribution function  $f(\xi, \mathbf{x}, t)$ , which reads (see Aidun & Clausen 2009)

$$\xi \frac{\partial f}{\partial \mathbf{x}} + \frac{\partial f}{\partial t} = \Theta. \quad (3.4)$$

Here,  $f(\xi, \mathbf{x}, t)$  is the probability to find a particle with velocity  $\xi$  at a position  $\mathbf{x}$  at a time  $t$ . The function  $f$  can be modified either by the motion of particles or by their collisions, which are determined by the collision operator  $\Theta$  in (3.4).

The lattice Boltzmann equation is a discretized form of the Boltzmann equation that emerges after a discretization of velocity, space and time. For an isotropic fluid the space can best be discretized by a uniform Cartesian grid. Velocity and time have to be discretized such that a particle travels from one grid point to a neighbouring grid point exactly in one time step. Different macroscopic velocities now correspond to different probability distributions of the particle velocities. A standard grid for modelling three-dimensional motions of this kind, shown in figure 2, is called a D3Q19 grid (Succi 2001) (D3: three-dimensional; Q19: 19 discrete velocities).

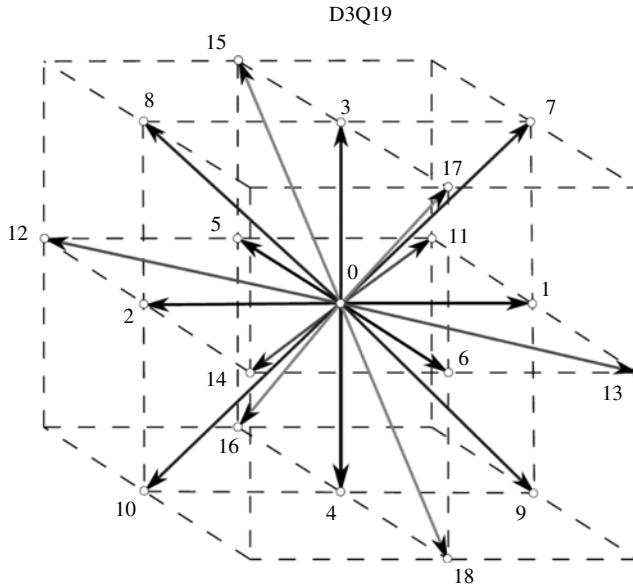


FIGURE 2. Grid structure and velocities with the D3Q19 discretization.

A crucial aspect in deriving the lattice Boltzmann equation is how to treat the collision operator  $\Theta$  in (3.4). A well-established approximation method is that by Bhatnagar, Gross and Kook (BGK) (Bhatnagar, Gross & Krook 1954) which models collisions as a relaxation to an equilibrium distribution function  $f_i^{eq}$ . With this approximation the lattice Boltzmann equation reads

$$f_i(\mathbf{x} + \xi_i \Delta t, t + \Delta t) - f_i(\mathbf{x}, t) = -\frac{1}{\tau} (f_i(\mathbf{x}, t) - f_i^{eq}(\mathbf{x}, t)), \tag{3.5}$$

$\tau$  is a relaxation time related to the fluid viscosity. The left-hand side of this equation represents the propagation of particles while the right-hand side describes the collisions. With an algorithm that executes these two steps, the collision step can be calculated after a propagation step on every grid point (Jin *et al.* 2015).

### 3.3. Accuracy of DNS methods

Direct numerical simulation solutions need numerical grids that are fine enough to resolve the smallest scales involved. Quite generally these smallest scales are of the order of the Kolmogorov scale:

$$\eta = \frac{\nu^{3/4}}{\varepsilon^{1/4}}, \tag{3.6}$$

where  $\nu$  is the kinematic viscosity of the fluid and  $\varepsilon$  is the local dissipation rate of the turbulent kinetic energy. This scale strongly depends on the Reynolds number (roughly  $\eta \sim Re^{-3/4}$ ) so that DNS solutions quite generally are restricted to moderate Reynolds numbers.

According to these considerations a perfect DNS solution would comply with the condition  $\Delta x_i / \eta \leq 1$ , where  $\Delta x_i$  ( $i = 1, 2, 3$ ) are the step sizes in the three dimensions of the solution domain. This, however, can hardly be achieved, especially very close

to the solid walls where the local dissipation rate  $\varepsilon$  is very large. One should also keep in mind that the Kolmogorov condition is a local statement about the numerical resolution. When  $\Delta x_i/\eta \leq 1$  cannot be met locally it is hard to say how this affects the solution further away or in the whole domain.

As an alternative measure of the overall accuracy of our solutions we introduced a quantity  $\Delta$ , called the accuracy measure, which we defined as

$$\Delta = \frac{g_p - g_s}{g_p}. \quad (3.7)$$

This was based on the following considerations. In fully developed flows, such as that through our GPM, the pressure gradient  $g_i$  in (3.2) can be determined in two ways, either by evaluating the pressure in two opposing cross-sections (we denoted this pressure gradient by  $g_p$ ) or by integrating the dissipation of mechanical energy between them,

$$g_s = \frac{2}{V_0 Re} \int_V s_{ij} s_{ij} dv, \quad (3.8)$$

where the non-dimensionalized strain rate is defined by  $s_{ij} = (\partial u_i/\partial x_j + \partial u_j/\partial x_i)/2$  and  $V_0$  is the volume of the computational domain.

For a perfect DNS solution the accuracy measure  $\Delta$  would be zero since in such a case  $g_p = g_s$ . In real DNS  $g_s$  will always be smaller than  $g_p$  since not all scales are resolved and certain local dissipation effects are missing. For example, the  $\Delta$  values are 0.1%–1.5% for the DNS results for a flow in a channel with smooth walls while they are 7%–10% for more complicated turbulent flows such as a flow in a channel with rough walls (see Jin & Herwig 2013, 2014).

For reasons explained later we start with low-resolution results, testing various parameter variations in §4, and then move on to high-resolution results in §5. Low and high resolution are determined with respect to the accuracy measure  $\Delta$ : low-resolution results are those with  $\Delta$  well above 10% while high-resolution results have  $\Delta$  values well below 10%.

#### 4. Low-resolution results

Since the main question in our study is whether large-scale turbulence occurs in porous medium flows, we (as a first step) determine the size of the REV-T with low-resolution DNS results. These solutions are obtained with numerical grids with step sizes  $\Delta x_i$ , for which  $\Delta x_i/\eta$  is larger than one in an appreciable part of the solution domain close to the walls and for which  $\Delta$ , defined by (3.7), is well above 10%. The underlying assumption is that the large-scale motion is not critically influenced by missing small scales. This assumption is supported by the generally small backscatter (energy transfer from small to large scales) in turbulent flows but nevertheless will be verified with the final solutions based on high-resolution results.

##### 4.1. Test cases 1–4

Taking into account the requirements with respect to the REV-T as well as the available computer resources we selected test cases 1–4 with parameter values according to table 1. We choose the obstacle size  $d$  as the length scale and refer all geometric parameters to  $d$ . Thus we do not fix the actual pore size but determine non-dimensional results. These results can be interpreted as different cases

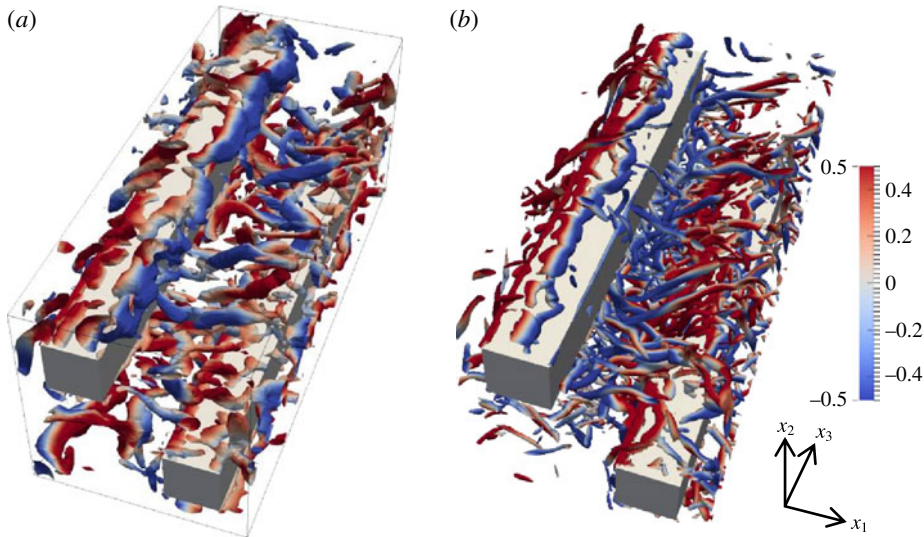


FIGURE 3. (Colour online) Flow field details in one REV-L element shown by isosurfaces  $Q \cdot d^2/u_m^2 = 10$ , colour coded with the instantaneous non-dimensional vertical velocity  $u_2$ . (a) Test case 1, FVM; (b) test case 4, LBM.

Test case	Pore size $s$	Domain size			Mesh resolution			Accuracy		
		$L_1$	$L_2$	$L_3$	$M_1$	$M_2$	$M_3$	$g_p$	$g_s$	$\Delta$ (%)
1	$2d$	$20d$	$20d$	$10d$	280	280	140	0.197	0.12	39
2	$2d$	$12d$	$8d$	$4d$	168	112	56	0.192	0.12	38
3	$2d$	$12d$	$4d$	$4d$	168	56	56	0.194	0.12	38
4	$2d$	$16d$	$16d$	$8d$	640	640	320	0.197	0.16	21

TABLE 1. Parameters of the test cases 1–4 (1–3: FVM; 4: LBM). Here,  $d$  is the size of the bars, see figure 1,  $Re = u_m d/\nu = 500$ ,  $s/d = 2$ ,  $\varphi = 0.88$  for all cases.

by assigning different values to the length  $d$ , for example  $d = 1$  mm or  $d = 0.1$  mm. All values are possible as long as the Navier–Stokes equations (which are solved in the incompressible limit assuming no slip at the solid boundaries) are an adequate theoretical model for the flow.

Figure 3 shows a turbulent flow structure in a part of the solution domain. Surfaces of constant values  $Q \cdot d^2/u_m^2 = 10$  shown in this figure represent the vortex structure. The quantity  $Q$  is the second invariant of the instantaneous velocity gradient tensor, which is defined by  $-\left((\partial u_i/\partial x_j)(\partial u_j/\partial x_i)\right)/2$  for an incompressible flow. Figure 3 shows that for this value of  $Q$  no large-scale structures can be identified; this also holds for larger  $Q$  values. Some of the turbulent structures may reach into neighbouring pores but they never extend far into the porous matrix. It should be noted that in figure 3 we show the same case ( $s/d = 2$  and  $Re = 500$ ) solved by the two DNS methods. Due to the relatively high resolution away from the walls the LBM results show more details of the small-scale structures compared with the FVM solution. Further details of the test case solutions are discussed in § 6 below.



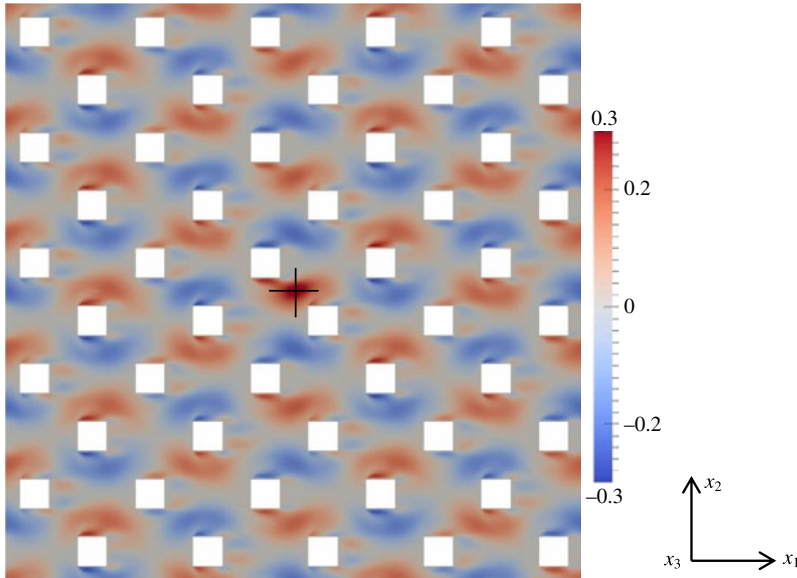


FIGURE 4. (Colour online) Two-point correlation  $R_{11}/u_m^2$  in the computational domain for test case 1. The correlation point  $\mathbf{x}_0$  is marked by the cross in the middle.

#### 4.2. Two-point correlations

One way to detect turbulent structures and analyse their scales is to determine two-point correlations in the flow field. By this technique one looks at two quantities of the same kind in the flow field which are a certain distance  $\mathbf{r}$  apart. When these quantities are subject to fluctuations (as in a turbulent flow), their fluctuations with respect to the corresponding time mean value  $\langle \dots \rangle$  will have positive and negative values alike.

When  $a$  is such a quantity, we write  $a = \langle a \rangle + a'$  with  $\langle a' \rangle = 0$  as a consequence of the splitting into time mean and fluctuating parts. When two such fluctuating quantities  $a_1$  and  $a_2$  are considered, we have  $\langle a'_1 \rangle = 0$  and  $\langle a'_2 \rangle = 0$ , but it is an open question how  $\langle a'_1 a'_2 \rangle$  would behave. When  $a_1$  and  $a_2$  are totally uncorrelated, the chances for  $a'_1 a'_2$  to be positive or negative are the same and thus  $\langle a'_1 a'_2 \rangle = 0$ . When, however, a physical correlation of whatever kind exists, there will be a non-zero value of  $\langle a'_1 a'_2 \rangle$  indicating this correlation.

The two-point correlation between the quantities  $a'_i(\mathbf{x})$  and  $a'_j(\mathbf{x}_0 + \mathbf{r})$  at a certain time  $t$  is called a two-point one-time autocovariance (Pope 2000) and it is defined as

$$R_{ij}(\mathbf{r}, \mathbf{x}_0) = \langle a'_i(\mathbf{x}, t) a'_j(\mathbf{x}_0 + \mathbf{r}, t) \rangle. \quad (4.1)$$

When  $u'_1(\mathbf{x}_0, t)$  and  $u'_1(\mathbf{x}_0 + \mathbf{r}, t)$  are correlated, we have

$$R_{11}(\mathbf{r}, \mathbf{x}_0) = \langle u'_1(\mathbf{x}_0, t) u'_1(\mathbf{x}_0 + \mathbf{r}, t) \rangle. \quad (4.2)$$

Figure 4 shows such correlation for test case 1 (see table 1) at  $\mathbf{x}_0 = (L_1/2, L_2/2, L_3/2)$ , i.e. in the middle of the computational domain with  $\mathbf{r}$  covering the whole  $(x_1, x_2)$  plane. From the colour coding it is evident that there is a strong correlation next to the point  $\mathbf{x}_0$ . However, there are also non-zero correlations around each obstacle irrespective of the distance to the correlation point  $\mathbf{x}_0$ . These correlations obviously appear due to the fact that a locally similar unsteady flow occurs around each of the

individual obstacles. The appearance of these correlations is not due to the interaction with turbulent structures at  $\mathbf{x}_0$ . Figure 3 shows that small turbulent structures build up around each obstacle, being confined to the pore of origin or its immediate vicinity. Thus, these small structures may affect the neighbouring pores but not those further away. Correlations in the far field are related to an almost two-dimensional vortex shedding blurred by turbulence, which occurs at all bars simultaneously. Figure 3(a,b) shows how such a vortex is formed all along the top bar. A similar kind of two-dimensional vortex shedding would also be found in laminar flow and, thus, we call the part of the two-point correlation that is not caused by turbulence a non-turbulent correlation.

The problem now is to distinguish the non-turbulent correlation from the true turbulent correlation that we are interested in. For this purpose we introduced a two-point lateral correlation, which for  $u'_1(\mathbf{x}_0, t)$  and  $u'_1(\mathbf{x}_0 + \mathbf{r}, t)$ , for example, is defined as

$$\tilde{R}_{11}(r_3, \mathbf{r}, \mathbf{x}_0) = \langle u'_1(\mathbf{x}_0, t)u'_1(\mathbf{x}_0 + \mathbf{r} + r_3\mathbf{e}_3, t) \rangle, \tag{4.3}$$

where  $\mathbf{e}_3$  is the unit vector in the  $x_3$  direction and  $\mathbf{r}$  is a vector within the  $(x_1, x_2)$  plane. Since it turned out that the non-turbulent correlation in the regular porous medium of our test cases is the same on all levels  $r_3$ , we can subtract  $\tilde{R}_{11}$  from  $R_{11}$  and obtain the turbulent correlation providing that  $r_3$  is sufficiently large. ‘Sufficiently large’ here means that the two correlation planes are sufficiently far apart so that there will be no correlation due to large-scale turbulent structures between them. Then  $\tilde{R}_{11}(r_3, \mathbf{r}, \mathbf{x}_0)$  according to (4.3) is the non-turbulent correlation.

Figure 5 shows  $(R_{11} - \tilde{R}_{11})$  distributions for increasing values of  $r_3$ . Once  $r_3$  is sufficiently large (here for  $r_3 \geq 1.5d$ ), there is no change in  $(R_{11} - \tilde{R}_{11})$  any more because then  $r_3$  exceeds the length scale of the largest turbulent interactions. What is left is the turbulent correlation:

$$\hat{R}_{11}(\mathbf{r}, \mathbf{x}_0) = R_{11}(\mathbf{r}, \mathbf{x}_0) - \tilde{R}_{11}(r_3 > r_{3c}, \mathbf{r}, \mathbf{x}_0), \tag{4.4}$$

where  $r_{3c}$  is the critical value of  $r_3$  up to which there is an influence of large-scale structures.

In §6.1 we will show  $R_{ij}$  and  $\tilde{R}_{ij}$  for high-resolution data, demonstrating that their difference (which is denoted by  $\hat{R}_{ij}$ ) is non-zero only where turbulent correlations occur.

Figure 6 shows three points within the flow field which are correlation points, with the point  $\mathbf{x}_0$  of figures 4 and 5 being one of them. The (similar) isosurfaces  $\hat{R}_{11}$  around these points show that the non-zero correlation extension is of the same order of magnitude (with  $\mathbf{x}_0$  having the largest area around it occupied by the same non-zero correlation values). This suggests that the point  $\mathbf{x}_0$  used thus far can indeed be taken as a representative correlation point.

#### 4.3. Parameter variations

The low-resolution results obtained thus far were for the pore size  $s/d = 2$  and the Reynolds number  $Re = 500$ . Both parameters should be varied systematically in order to determine their influence. We did this according to table 2, introducing the case labelling A–F.

So far case A has been determined in terms of low-resolution results; see table 1 for the four test cases of this category. In table 3 low-resolution solutions are shown

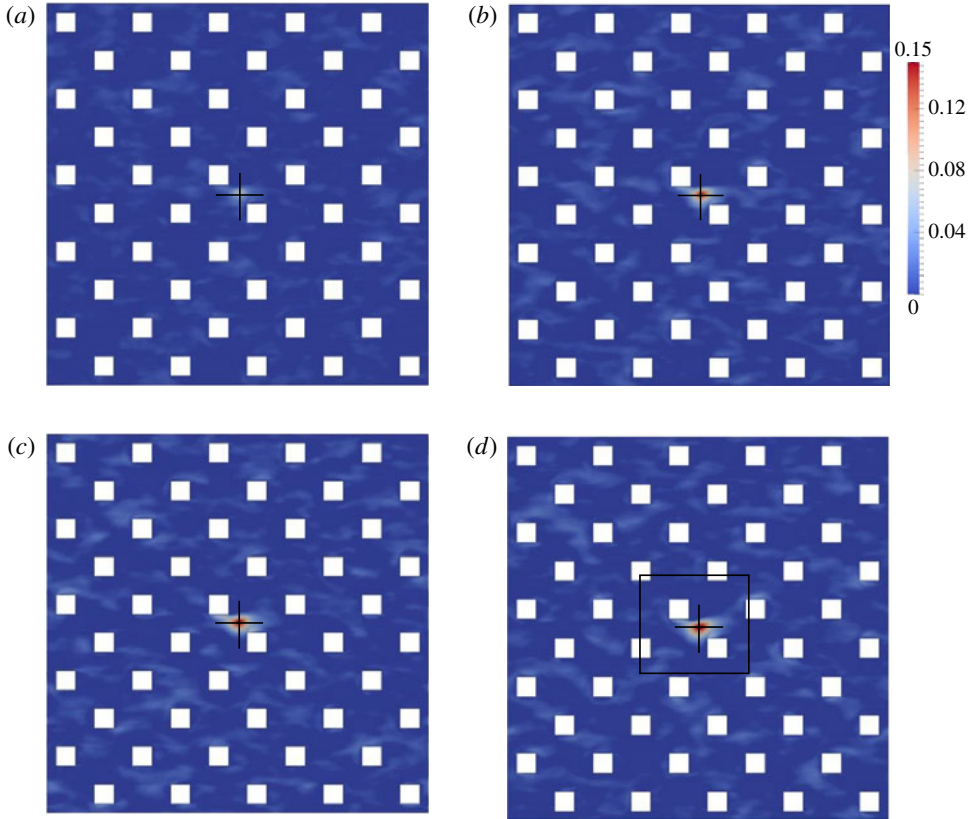


FIGURE 5. (Colour online) Plots of  $(R_{11} - \tilde{R}_{11})/u_m^2$  for different  $r_3$  in the computational domain for test case 1 ( $Re = 500$ ,  $s/d = 2$ ). The correlation point  $\mathbf{x}_0$  is marked by the cross in the middle. The zoomed contours inside the frame of figure 5(d) are shown in figure 6. (a)  $r_3 = 0.2d$ ; (b)  $r_3 = 0.5d$ ; (c)  $r_3 = 1.5d$ ; (d)  $r_3 = 5d = L_3/2$ .

for cases B–E, determined by the FVM approach. So far only the accuracy measures  $\Delta$  are given. Details of the solutions will be discussed in §6 below. Case F with the highest Reynolds number will be calculated only with high resolution after the trends of parameter influences for the five cases A–E have been determined.

#### 4.4. Size determination for REV-T

As argued at the beginning of §4, the minimum size of the REV-T can be determined from the low-resolution results and then used for the high-resolution calculations. On analysing the solutions obtained so far and especially looking at figure 5 it is evident that in all three directions only a few pore sizes  $s$  are needed in order to define a solution domain large enough to avoid the suppression of large-scale turbulent structures. For further clarification, figure 7 shows the two-point correlations  $R_{11}$ ,  $R_{22}$  and  $R_{33}$  according to (4.1) of the three velocity fluctuation components  $u'_1$ ,  $u'_2$  and  $u'_3$  in a plane  $x_1 = L_1/2$ , for test case 1 in table 1. While  $R_{11}$  and  $R_{22}$  show correlations for velocities perpendicular to the bars of the porous matrix (and thus show a repeating pattern),  $R_{33}$  is the correlation of a velocity component along the bars.

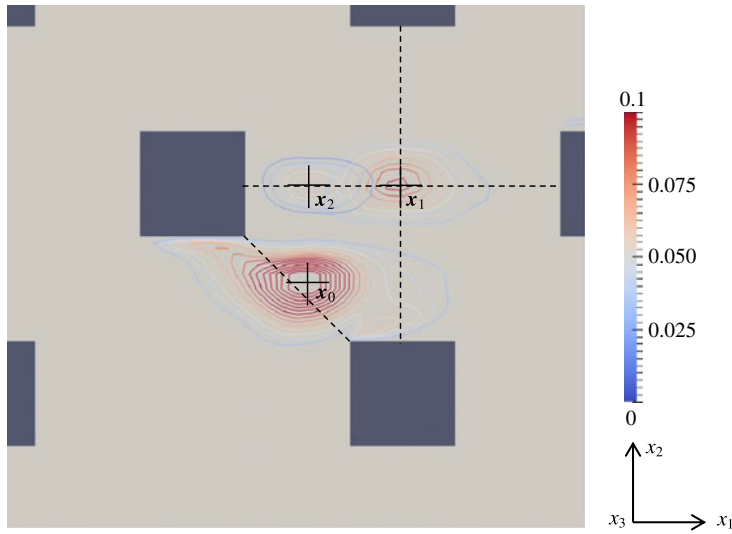


FIGURE 6. (Colour online) Isosurfaces of  $\hat{R}_{11}/u_m^2$  at three points; decreasing values for increasing distance from the correlation points, see the colour coding.

$Re = 500$			$s/d = 2$ ( $\varphi = 0.88$ )		
Pore size variation			Reynolds number variation		
$s/d = 2$ ( $\varphi = 0.88$ )	$s/d = 3$ ( $\varphi = 0.94$ )	$s/d = 1.5$ ( $\varphi = 0.78$ )	$Re = 600$	$Re = 700$	$Re = 1000$
A	B	C	D	E	F

TABLE 2. Cases A–F for different pore sizes and Reynolds numbers. The test cases in table 1 all belong to case A.

Test case	Pore size $s$	$Re$	Domain size			Mesh resolution			$g$	$g_s$	$\Delta$ (%)
			$L_1$	$L_2$	$L_3$	$M_1$	$M_2$	$M_3$			
B	$3d$	500	$30d$	$30d$	$10d$	420	420	150	0.066	0.047	29
C	$1.5d$	500	$15d$	$15d$	$6d$	600	600	150	0.890	0.682	23.4
D	$2d$	600	$20d$	$20d$	$10d$	320	320	150	0.198	0.122	38
E	$2d$	700	$20d$	$20d$	$10d$	360	360	150	0.199	0.118	41

TABLE 3. Cases B–E, low resolution (FVM).

In all three directions the limited range of the non-zero correlation values is clearly visible. Since the periodic boundary conditions on the domain boundaries are an unphysical constraint in the numerical solution process, we choose minimum solution domain sizes conservatively, to be ‘on the safe side’. Thus,  $L_3/d$  can be set to a rather low value ( $L_3/d = 4$ ) for all subsequent calculations, see figure 7(a), where a  $4d$  spacing is indicated by the two vertical lines. This is in accordance with a suggestion by Afgan *et al.* (2011), who also set  $L_3/d = 4$  for simulations of a flow around a single cylinder or around two parallel cylinders. In the other two directions high-resolution results will be determined with  $L_1/s = 6$  and  $L_2/s = 4$ .

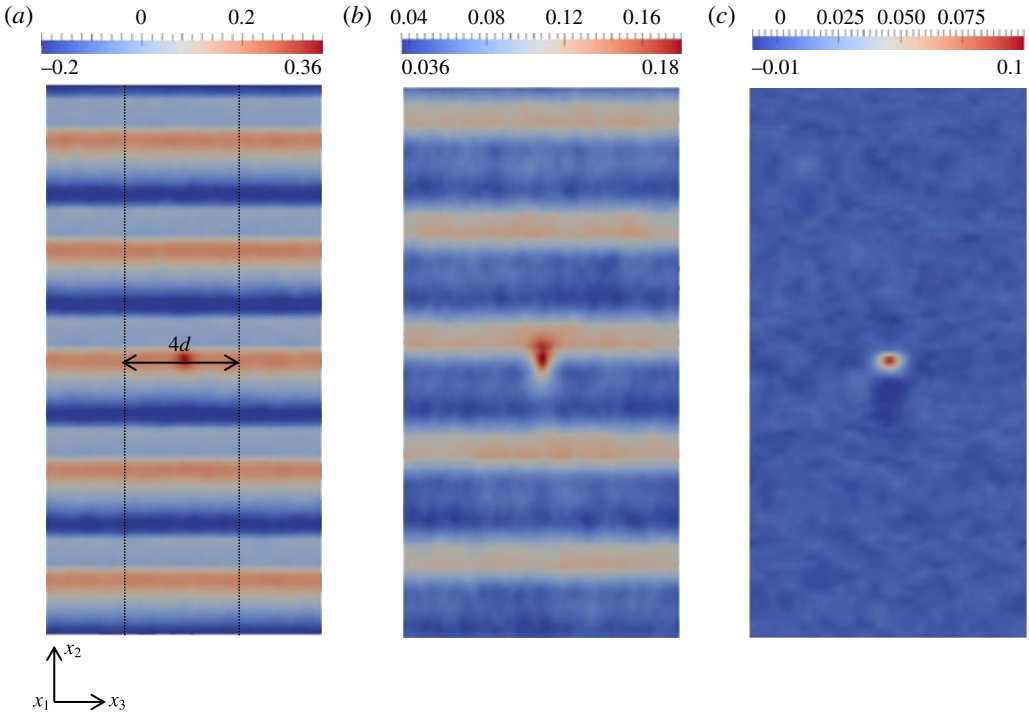


FIGURE 7. (Colour online) Two-point correlations in the plane  $x_1 = L_1/2$  for test case 1, see table 1: (a)  $R_{11}/u_m^2$ ; (b)  $R_{22}/u_m^2$ ; (c)  $R_{33}/u_m^2$ .

## 5. High-resolution results

In table 4 parameters and pressure gradient results of all high-resolution solutions are given, including the mesh resolution and accuracy measures for the FVM and LBM approaches respectively.

The domain size for all cases is such that  $L_1/s = 6$  and  $L_2/s = 4$ , so that for all cases there are 12 bars in the solution domain. Not all cases have been calculated with both methods; those for higher Reynolds numbers have been determined either by the FVM or by the LBM approach due to limited computer resources. Here, 36–123 million grid points were used in the FVM cases while 100–384 million grid points were used in the LBM cases. All calculations were performed at the North Germany Supercomputing Alliance (HLRN/Norddeutscher Verbund zur Förderung des Hoch- und Höchstleistungsrechnens) with 480 processors of the Cray XC30. The CPU time (processor number  $\times$  computing time) for one test case in table 4 varied between 25 000 and 58 000 h. More details with respect to the mesh resolution, time step and other computational details are given in appendix A.

The accuracy measure  $\Delta$  shows values  $< 10\%$ , which has been set as the criterion for high-resolution results, see the end of § 3.3. The only exception from this rule is case C/FVM with  $\Delta = 11.1\%$ . Since this is the case with the lowest value of  $s/d$ , the solution domain has the highest portion of near-wall areas. This is where DNS solutions cannot always meet the Kolmogorov condition  $\Delta x_i/\eta < 1$ , so that more small-scale motions are missing in the integration of the local entropy generation (which leads to  $g_s$ ) than in the other cases in table 4.

Case	Method	$s/d$	$Re$	Domain size			Mesh resolution			Accuracy		
				$L_1/d$	$L_2/d$	$L_3/d$	$M_1$	$M_2$	$M_3$	$g_p$	$g_s$	$\Delta$ (%)
A	FVM	2	500	12	8	4	720	480	150	0.190	0.180	5.3
	LBM	2	500	12	8	4	768	512	256	0.196	0.177	9.7
B	FVM	3	500	18	12	4	960	640	150	0.052	0.051	2.9
	LBM	3	500	18	12	4	1152	768	256	0.052	0.048	7.7
C	FVM	1.5	500	9	6	4	600	400	150	0.900	0.800	11.1
	LBM	1.5	500	9	6	4	900	600	400	0.900	0.830	7.8
D	FVM	2	600	12	8	4	840	560	180	0.190	0.180	5.3
	LBM	—	—	—	—	—	—	—	—	—	—	—
E	FVM	2	700	12	8	4	960	640	200	0.188	0.176	6.4
	LBM	—	—	—	—	—	—	—	—	—	—	—
F	FVM	—	—	—	—	—	—	—	—	—	—	—
	LBM	2	1000	12	8	4	1200	800	400	0.185	0.170	5.6

TABLE 4. Cases A–F, high resolution.

Details of the solutions given in table 4 will be used in § 6. As an example, one snapshot of the instantaneous flow field in a part of the solution domain for case F with  $Re = 1000$  is shown in figure 8. The vortical structures are identified by the isosurfaces of  $Q$ , now with  $Q \cdot d^2/u_m^2 = 1$ . Most of the large vortices have the same length scale as the pore size  $s$  (figure 8). The vortices in one REV-L element may have a slight influence only on the neighbouring elements.

## 6. Discussion of the results

All results obtained in this study will now be discussed with respect to the following two crucial questions.

- (i) Is there macroscopic turbulence in porous media?
- (ii) Can low-resolution DNS results be used to answer fundamental questions (like the one above)?

We will give a direct answer to the first question and indirectly address the second one. Both questions will be addressed by considering three aspects of the turbulent flow through porous media in the following three subsections.

### 6.1. Two-point turbulent correlations

Two-point correlations  $\hat{R}_{ii} = R_{ii} - \tilde{R}_{ii}$  as a generalization of the two-point correlation  $\hat{R}_{11} = R_{11} - \tilde{R}_{11}$  (see (4.4)) are characteristic quantities with respect to the range of impact of turbulent structures referred to a certain point  $\mathbf{x}_0$  in the flow field. So far they have been shown by colour coding in figures 5 and 7. A more accurate presentation will be given from now on in terms of  $\hat{R}_{ii}$  distributions along a certain line in the flow field. According to their definitions (see (4.2) and (4.3) which define  $R_{11}$  and  $\tilde{R}_{11}$  respectively), the two correlations  $R_{ii}$  and  $\tilde{R}_{ii}$  will differ from each other only when there are turbulent correlations in addition to the non-turbulent correlations. This means that when turbulent correlations vanish at large distances

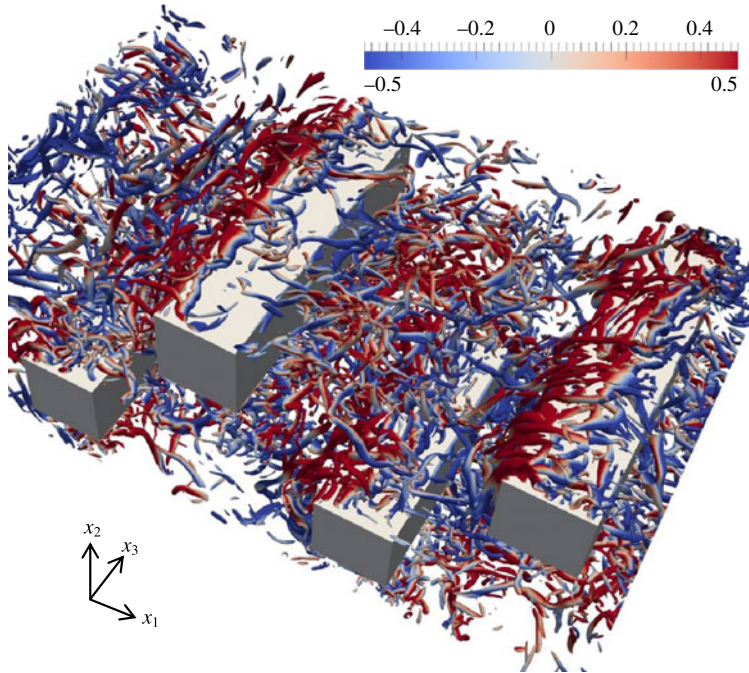


FIGURE 8. (Colour online) Snapshot of parts of the flow field in two REV-L elements, case F ( $Re = 1000$ ,  $s/d = 2$ ), isosurfaces  $Q \cdot d^2/u_m^2 = 1$ , colour coding with the instantaneous vertical velocity  $u_2$ .

from the correlation point,  $R_{ii}$  and  $\tilde{R}_{ii}$  become equal. Figure 9 shows three two-point correlations,  $R_{11}$ ,  $R_{22}$  and  $R_{33}$ , as well as the corresponding two-point non-turbulent correlations,  $\tilde{R}_{11}$ ,  $\tilde{R}_{22}$  and  $\tilde{R}_{33}$ , in both directions (see figure 9a–c for the streamwise direction and figure 9d–f for the transverse  $x_2$  direction). Outside one pore size  $R_{ii}$  and  $\tilde{R}_{ii}$  are virtually equal, which in figures 10–13 for  $\hat{R}_{ii} = R_{ii} - \tilde{R}_{ii}$  leads to zero values of  $\hat{R}_{ii}$  for distances greater than  $s$  away from the correlation point.

In figure 10 we show that the typical correlations  $\hat{R}_{ii}$  in the streamwise direction ( $x_1$  direction) and in the transverse direction ( $x_2$  direction) are very similar, at least with respect to the range of non-zero values. They all are virtually zero beyond  $|(x_i - x_{i0})|/s > 1$ , i.e. they drop to zero over a length of one pore scale  $s$ , indicating that the largest turbulent structures are of that size. Small non-zero values may occur when some turbulent structures reach into neighbouring pores.

Figure 11 shows  $\hat{R}_{ii}$  for the same parameter values,  $Re = 500$  and  $s/d = 2$ , but for different sizes of the solution domain. They are those of the test cases 1–3, see table 1, and in addition two cases with even smaller domain sizes ( $8d \times 8d \times 4d$  and  $4d \times 4d \times 4d$ ). For all five cases the  $\hat{R}_{ii}$  distributions are very similar, which confirms our assumption of being on the safe side with our choice of the domain size for the high-resolution cases A–F in table 4.

Figure 12 shows the effect of a variation of the pore size (or porosity), while figure 13 shows the effect of a Reynolds number variation. Variations of either parameter only marginally influence the  $\hat{R}_{ii}$  distributions. With an increasing pore size  $s$  (or porosity  $\phi$ ), the distributions of  $\hat{R}_{22}$  and  $\hat{R}_{33}$  in the  $x_1$  direction become

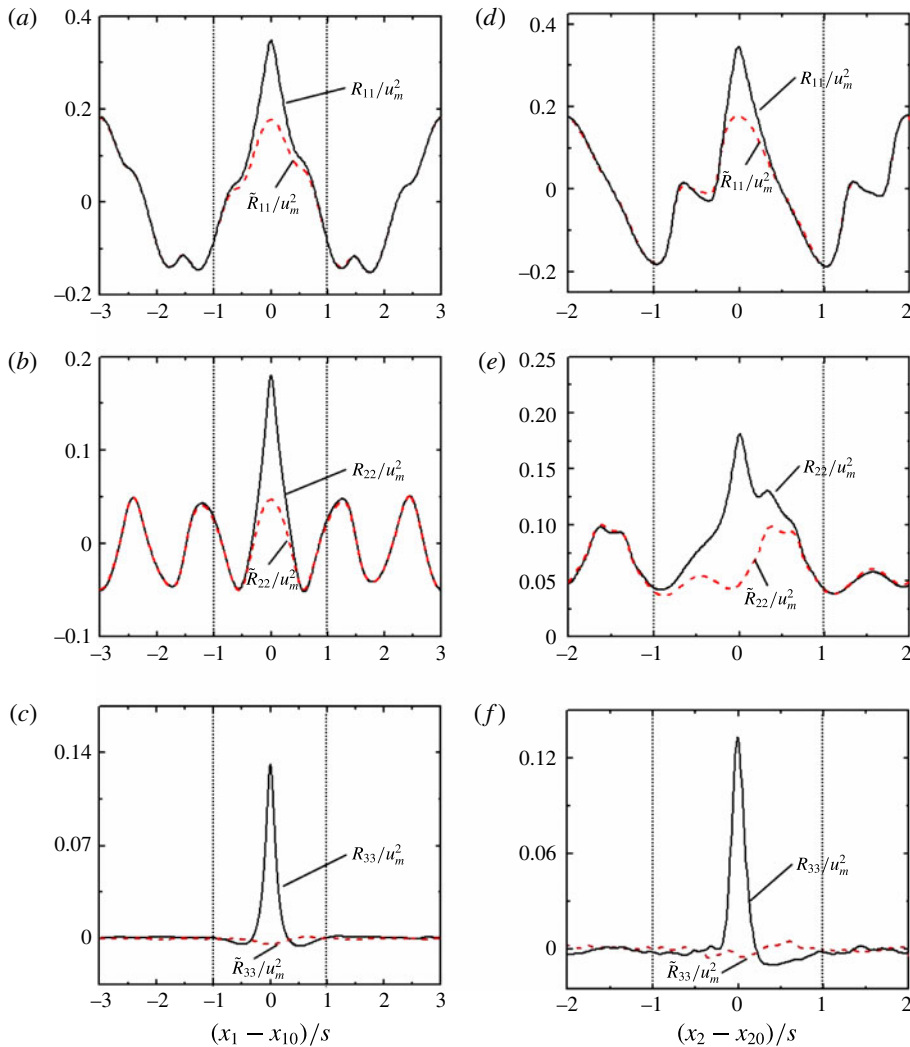


FIGURE 9. (Colour online) Two-point and non-turbulent two-point correlations in the streamwise direction (a–c) and transverse  $x_2$  direction (d–f). The reference point is in the centre of the solution domain  $(x_{10}, x_{20})$ ,  $Re = 500$ ,  $s/d = 2$ , high-resolution LBM results. Here, — indicates two-point correlations; --- indicates non-turbulent two-point correlations.

slightly wider. However, their non-zero values are still only found in the REV-L domain, which means that  $|x_1 - x_{10}| \leq s$  (see figure 12b,c). Altogether, the two-point correlations indicate that the scales of the turbulent structures are of the pore size  $s$ .

### 6.2. Integral length scales

Another way to quantify the size of large eddies is to determine their integral length scales. These length scales are defined as longitudinal, transverse and spanwise lengths  $L_{ii}$ , similar to the definitions in Pope (2000) for homogeneous and isotropic turbulent



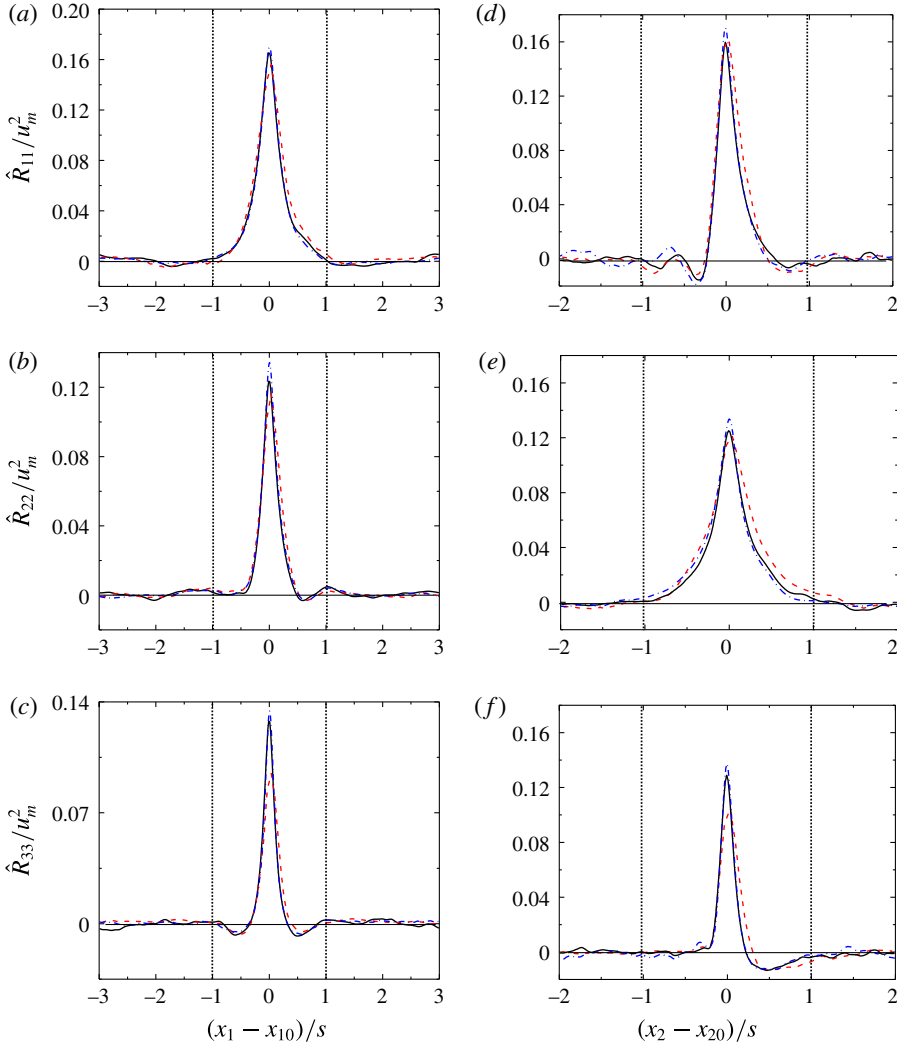


FIGURE 10. (Colour online) Turbulent two-point correlations in the streamwise direction (a–c) and transverse  $x_2$  direction (e–f). The reference point is in the centre of the solution domain  $(x_{10}, x_{20})$ , the domain size is  $6s \times 4s \times 4d$ ,  $Re = 500$ ,  $s/d = 2$ . Here, — indicates high-resolution FVM results, case A, see table 4; --- indicates low-resolution FVM results, test case 2, see table 1; - · - · - indicates high-resolution LBM results, case A, see table 4.

flows:

$$L_{11} = \int_{-\infty}^{\infty} \hat{R}_{11}(r_1 \mathbf{e}_1, \mathbf{x}_0) / \hat{u}_1^2(\mathbf{x}_0) dr_1, \tag{6.1}$$

$$L_{22} = \int_{-\infty}^{\infty} \hat{R}_{22}(r_1 \mathbf{e}_1, \mathbf{x}_0) / \hat{u}_2^2(\mathbf{x}_0) dr_1, \tag{6.2}$$

$$L_{33} = \int_{-\infty}^{\infty} \hat{R}_{33}(r_1 \mathbf{e}_1, \mathbf{x}_0) / \hat{u}_3^2(r_0) dx_1, \tag{6.3}$$

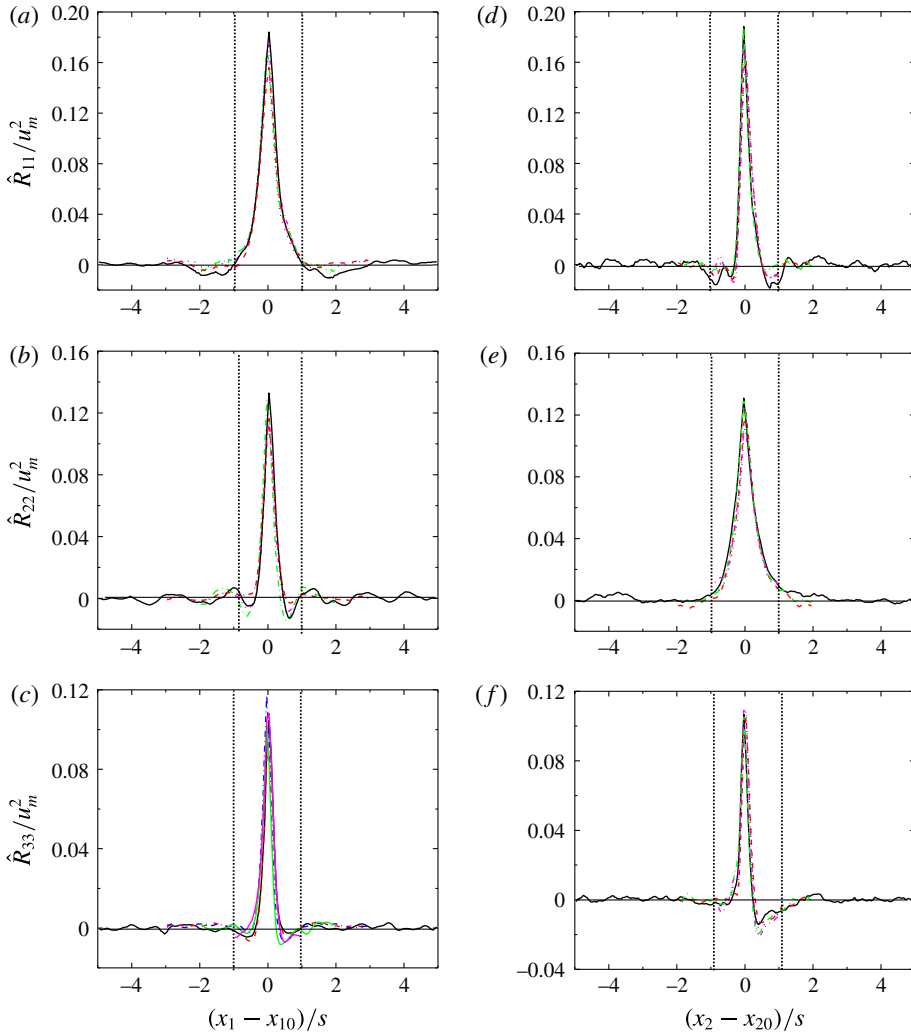


FIGURE 11. (Colour online) Turbulent two-point correlations in the streamwise direction (a–c) and transverse  $x_2$  direction (e–f). The reference point is in the centre of the solution domain  $(x_{10}, x_{20})$ ,  $Re = 500$ ,  $s/d = 2$ , low-resolution FVM results. Various line types indicate different domain size  $L_1 \times L_2 \times L_3$ . Here, — indicates  $20d \times 20d \times 10d$ , --- indicates  $12d \times 8d \times 4d$  and ..... indicates  $12d \times 4d \times 4d$ , i.e. test cases 1–3 respectively (table 1); - · - · - indicates  $8d \times 8d \times 4d$  and — · — indicates  $4d \times 4d \times 4d$ .

where  $\hat{u}'_i(\mathbf{x}_0)$  is the root-mean-square (r.m.s.) turbulent velocity component, which can be calculated as

$$\hat{u}'_i(\mathbf{x}_0) = \hat{R}_{ii}(0, \mathbf{x}_0)^{1/2}. \tag{6.4}$$

We use these definitions despite the fact that the flow through porous media is not one with isotropic and homogeneous turbulence. However, since we are only interested in the order of magnitude of these length scales (pore or domain size), we assumed that the  $L_{ii}$  length scales obtained from (6.1)–(6.3) are of the same order of magnitude as the corresponding length scales of the non-isotropic turbulence prevailing in porous medium flows.

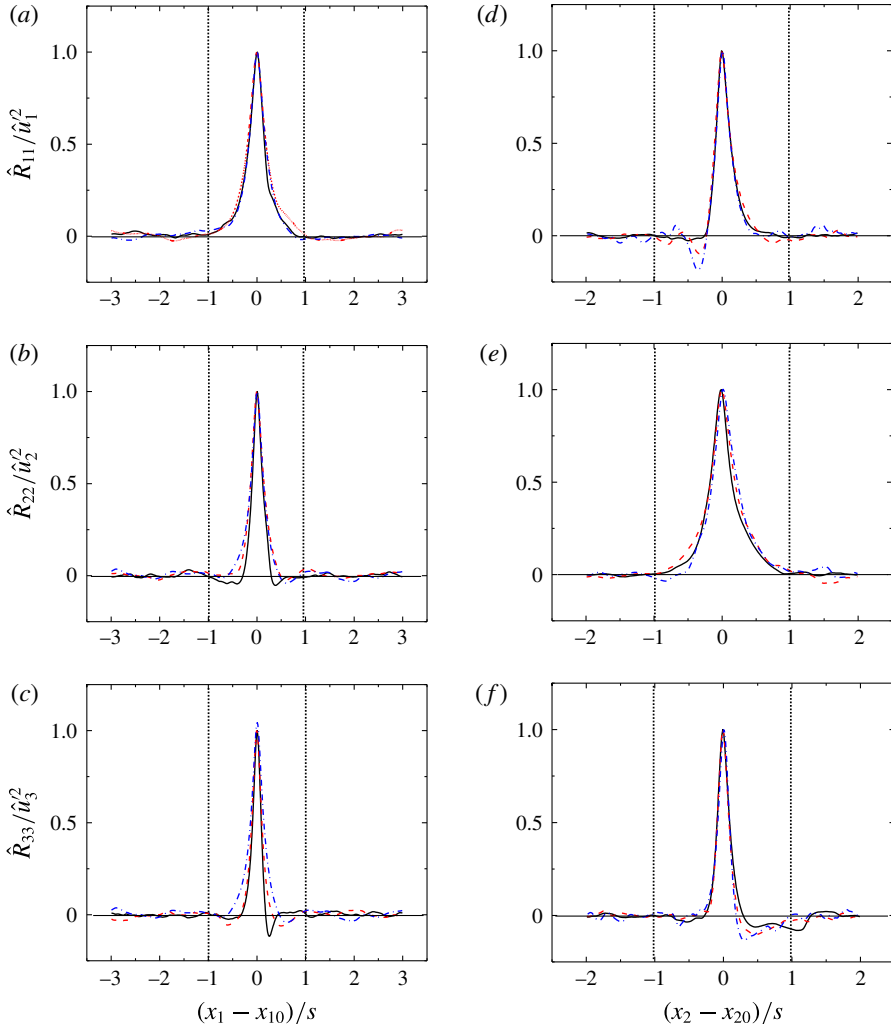


FIGURE 12. (Colour online) Turbulent two-point correlations in the streamwise direction (a–c) and transverse  $x_2$  direction (e–f). The reference point is in the centre of the solution domain  $(x_{10}, x_{20})$ , pore size variations,  $Re = 500$ , high-resolution FVM results. Here, — indicates  $s/d = 1.5$  ( $\varphi = 0.78$ , case C/FVM), --- indicates  $s/d = 2$  ( $\varphi = 0.88$ , case A/FVM) and -·-·- indicates  $s/d = 3$  ( $\varphi = 0.94$ , case B/FVM).

Table 5 gives length scale values for all cases A–F from table 4 (high-resolution results), non-dimensionalized with the pore scale  $s$ . The length scale  $L_{11}/s$  is larger than the other two length scales for all the cases. As the pore size  $s$  is increased from  $1.5d$  to  $3d$  (or the porosity  $\varphi$  is increased from 0.78 to 0.94), the values of  $L_{22}/s$  and  $L_{33}/s$  increase moderately, but they are still smaller than 1 (see these values for cases B/FVM and C/FVM in table 5). Altogether, the integral length scale data again indicate that the scales of the turbulent structures are of the pore size  $s$ .

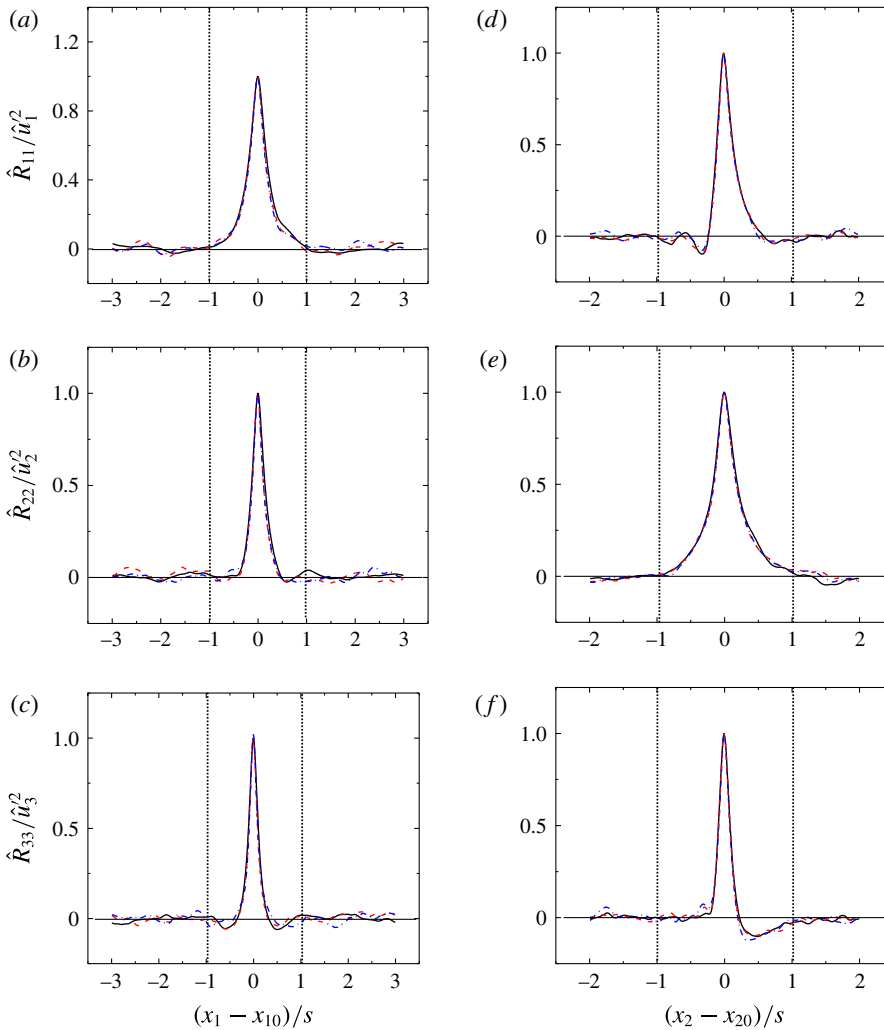


FIGURE 13. (Colour online) Turbulent two-point correlations in the streamwise direction (a–c) and transverse  $x_2$  direction (e–f). The reference point is in the centre of the solution domain  $(x_{10}, x_{20})$ , Reynolds number variations,  $s/d = 2$ , high-resolution FVM results. Here, — indicates  $Re = 500$  (case A/FVM), --- indicates  $Re = 600$  (case D/FVM) and - · - · - indicates  $Re = 700$  (case E/FVM).

### 6.3. Energy spectra and their premultiplied form

For sufficiently high Reynolds numbers energy spectra have been derived by Kolmogorov (1941) under the assumption of locally homogeneous and isotropic turbulence being statistically in equilibrium. They are

$$\hat{E}_{ii}(\mathbf{x}_0, k_1) = \frac{1}{\pi} \int_{-\infty}^{\infty} \hat{R}_{ii}(x_1 \mathbf{e}_1, \mathbf{x}_0) \exp(-ik_1 x_1) dx_1. \quad (6.5)$$

Again, as an approximation, we use this definition, although the flow through porous media is not one with isotropic and homogeneous turbulence. Figure 14 shows these

Case	$s/d$	$\varphi$	$Re$	$L_{11}/s$	$L_{22}/s$	$L_{33}/s$
A/FVM	2	0.88	500	0.52	0.36	0.21
A/LBM	2	0.88	500	0.50	0.35	0.24
B/FVM	3	0.94	500	0.48	0.35	0.37
C/FVM	1.5	0.78	500	0.46	0.22	0.18
D/FVM	2	0.88	600	0.50	0.31	0.22
E/FVM	2	0.88	700	0.47	0.30	0.20
F/LBM	2	0.88	1000	0.41	0.28	0.17

TABLE 5. Integral length scales assuming isotropic flow, obtained from (6.1)–(6.3).

spectra for the low Reynolds number  $Re = 500$  and  $s/d = 2$  for three solutions. An indication of a sufficiently high Reynolds number is a distinct inertia range with a slope of  $-5/3$ , shown by the straight lines in figure 14. Figure 15(a–c) shows that this region becomes more pronounced for larger Reynolds numbers, when  $Re$  is increased from 500 to 1000.

The energy spectra in figure 15(a–c) are multiplied by  $k_1 s$  and plotted on semi-logarithmic axes in figure 15(d–f); these are also called premultiplied energy spectra. For pipe/channel flows, Jimenez (1998) suggests the use of this type of plot to identify the  $k_1^{-1}$  range, in which  $k_1 \hat{E}_{11} \approx \text{constant}$ . Guala, Hommema & Adrian (2006) and Balakumar & Adrian (2007) indicate that two peaks in the  $k_1^{-1}$  range represent the very-large-scale motions (VLSMs) which have the maximum wavelength and the large-scale motions (LSM) which have the minimum wavelength.

In our study, a region of  $k_1 \hat{E}_{11} \approx \text{constant}$  can also be found (see figure 15d), which may indicate the range of large-scale turbulent motions. The peak of  $k_1 \hat{E}_{11}$  with the maximum wavelength of  $\Lambda = 2\pi/k_1 \approx 2s$  (the corresponding wavenumber  $k_1 \approx 3/s$ ), which is the same as the size of an REV-L element. With increasing Reynolds number, the energy carried by large-scale motions becomes lower, suggesting that the large-scale turbulence motions are even less important at larger  $Re$ . The maximum wavelengths corresponding to the peaks for  $k_1 \hat{E}_{22}$  and  $k_1 \hat{E}_{33}$  are approximately  $1.25s$ .

The effects of the pore size  $s$  (or porosity  $\varphi$ ) on the energy spectra and the premultiplied energy spectra are shown in figure 16. Similar inertia ranges can be observed in all three test cases (see figure 16a–c). As the pore size  $s$  is increased from  $1.5d$  to  $3d$  (or porosity  $\varphi$  is increased from 0.78 to 0.94), the maximum wavelengths corresponding to the peaks for  $k_1 \hat{E}_{11}$ ,  $k_1 \hat{E}_{22}$  and  $k_1 \hat{E}_{33}$  are slightly increased (see figure 16d–f), but they never exceed the size of an REV-L element,  $2s$ . Altogether, the energy spectra data support the previous findings that turbulent structures are of the pore size scale  $s$ .

## 7. Conclusions

We believe that the results obtained in this study can provide the answer to the question of whether or not macroscopic turbulence exists in porous media, even though a special generic matrix was defined and used in all calculations. The underlying assumption is that there is no fundamental qualitatively different flow behaviour when the porous matrix is changed from two-dimensional regular to three-dimensional irregular geometry. As we have shown, the pore size restricts the size of turbulent structures even in a two-dimensional matrix unrestricted in

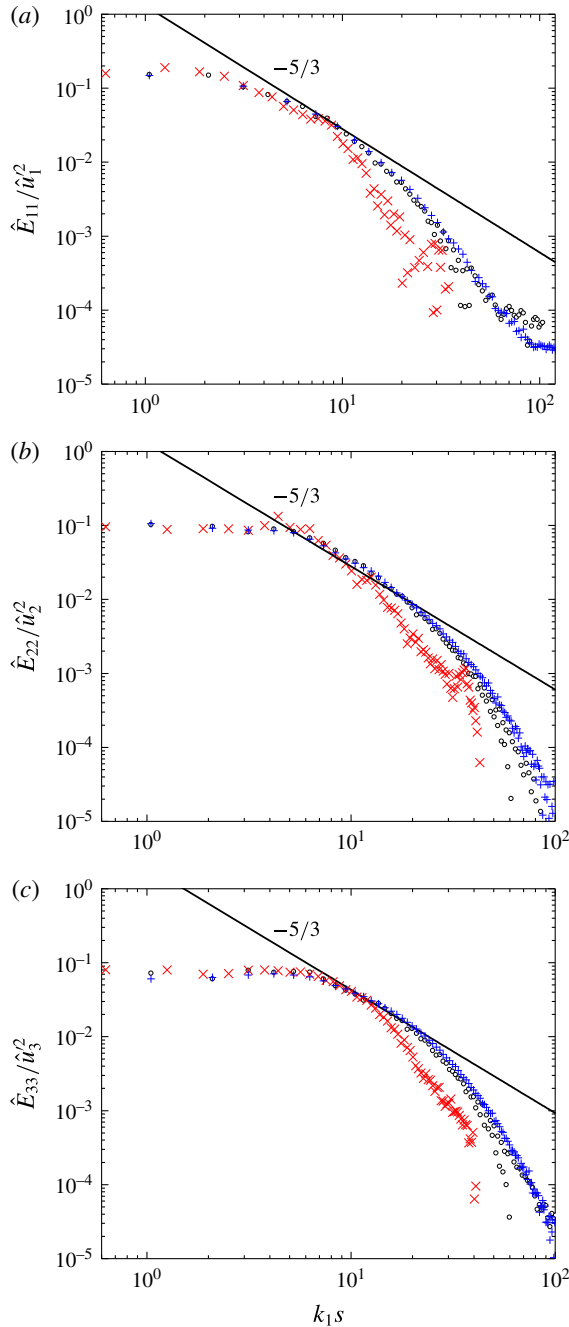


FIGURE 14. (Colour online) Energy spectra of the turbulent motions obtained from (6.5) for different cases,  $Re = 500$ ,  $s/d = 2$ :  $\circ \circ \circ \circ \circ$ , high-resolution FVM results, case A (table 4);  $\times \times \times \times \times$ , low-resolution FVM results, case 2 (table 1);  $+++++$ , high-resolution LBM results, case A (table 4).

the third dimension. We expect that a three-dimensional matrix will not weaken or even eliminate these restrictions on the size of turbulent structures. Irregularities in pore sizes and shapes may lead to locally different restrictions but not to their

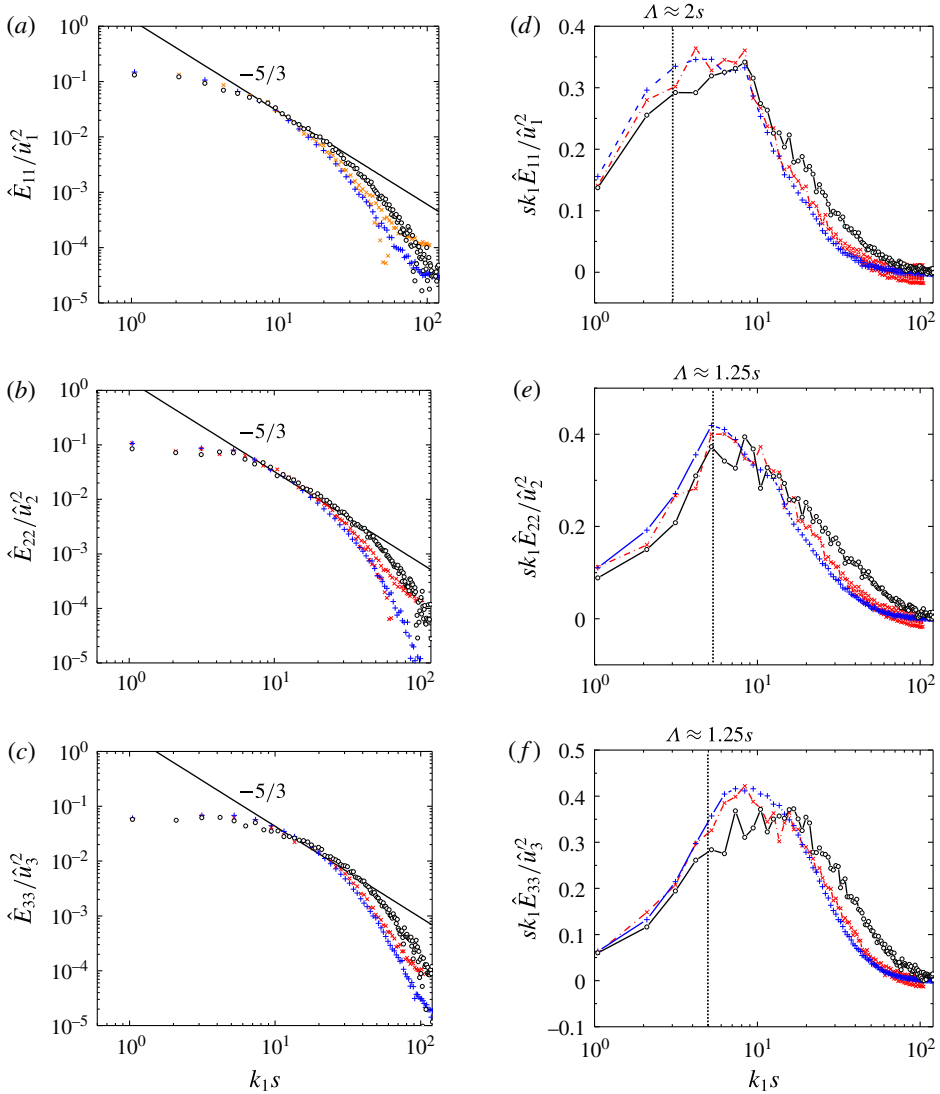


FIGURE 15. (Colour online) Energy spectra of the turbulent motions according to (6.5) for increasing Reynolds numbers;  $s/d = 2$ , high-resolution results. (a–c) Energy spectra; (d–f) premultiplied energy spectra; +++++,  $Re = 500$  (case A/LBM); xxxxxx,  $Re = 700$  (case E/FVM); oooooo,  $Re = 1000$  (case F/LBM).

disappearance as a whole. Our porous matrix is not very tortuous; its tortuosity is close to unity. However, we expect that increasing tortuosity will further dampen any possible macroscopic turbulence.

The analysis of all DNS data obtained in this study shows that the sizes of turbulent structures do not extend far beyond the pore scale. This agrees with the prediction made in Nield (1991) and asserted in Nield & Bejan (1992, p. 8). We further found that certain turbulent structures may have a slight impact on immediately neighbouring pores. This impact, however, decays further away so that no large-scale structures prevail. This statement is in accordance with all two-point correlation data (see figures

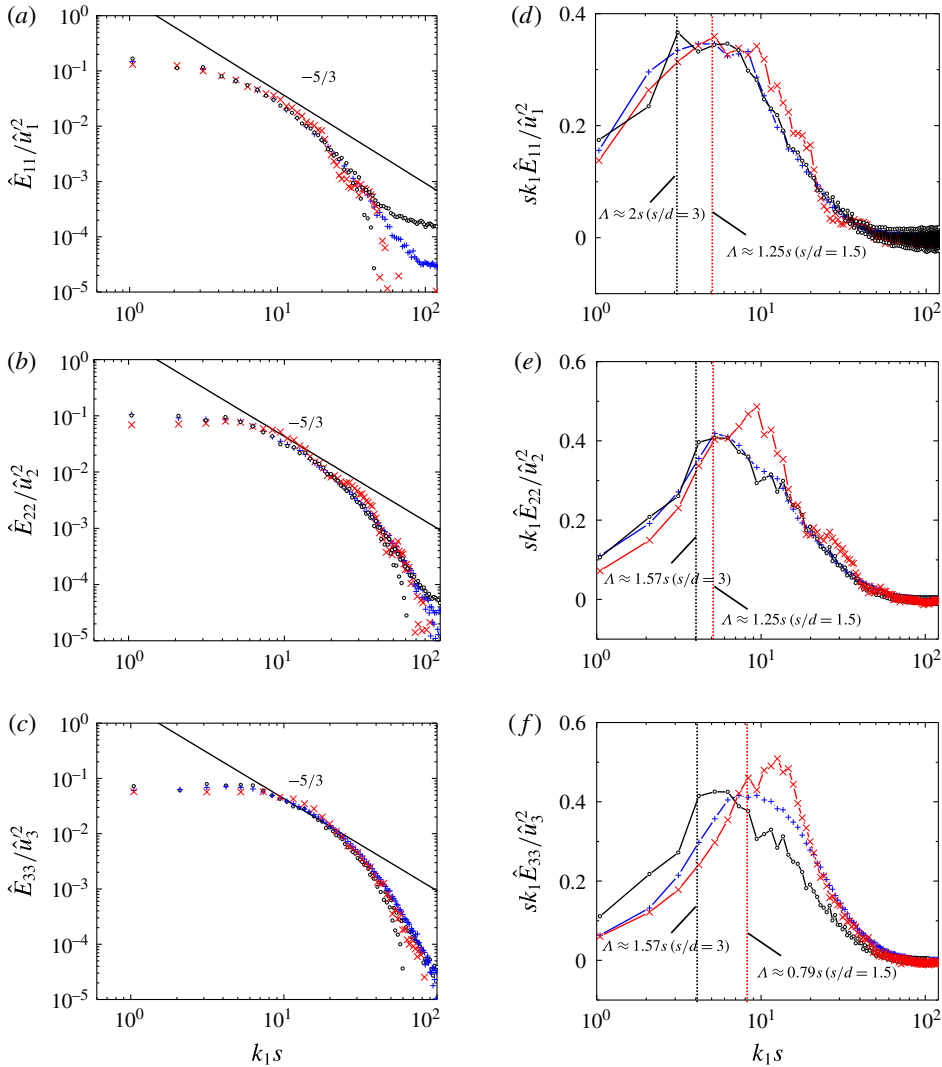


FIGURE 16. (Colour online) Energy spectra of the turbulent motions according to (6.5) for different pore sizes;  $Re = 500$ , high-resolution results. (a–c) Energy spectra; (d–f) premultiplied energy spectra;  $\times\times\times\times\times$ ,  $s/d = 1.5$  ( $\varphi = 0.78$ , case A/FVM);  $+++++$ ,  $s/d = 2$  ( $\varphi = 0.88$ , case A/LBM);  $\circ\circ\circ\circ\circ$ ,  $s/d = 3$  ( $\varphi = 0.94$ , case FVM).

5 and 10–13), all approximate integral length scale data (see table 5) and all energy spectrum data (see figure 14). This general finding is visualized by the snapshot in figure 8 showing turbulent structures of various sizes, all of them limited in their extension to values well beyond the pore scale  $s$ .

Our low- and high-resolution DNS results also show that missing the turbulent fine scales due to an insufficient numerical resolution nevertheless allows conclusions about the large turbulent scales. Obviously, turbulent backscatter is weak so that, for example, the two-point correlations for the case A/FVM with the accuracy measure  $\Delta = 5.3\%$  are similar to those of the test case 2 with  $\Delta = 38\%$ , as can be seen in figure 10. Details such as the high-wavenumber energy content, however, are very



Test case	$(\Delta x_1/d)_c$	$(\Delta x_1/d)_w$	$(\Delta x_2/d)_c$	$(\Delta x_2/d)_w$	$\Delta x_3/d$
(a) Low-resolution FVM cases (cf. table 3)					
A	0.13	0.026	0.13	0.026	0.071
B	0.14	0.028	0.14	0.028	0.067
C	0.10	0.020	0.01	0.020	0.040
D	0.11	0.022	0.11	0.022	0.071
E	0.10	0.020	0.10	0.020	0.071
(b) High-resolution FVM cases (cf. table 4)					
A	0.032	0.0064	0.032	0.0032	0.027
B	0.039	0.0078	0.039	0.0078	0.027
C	0.024	0.0048	0.024	0.0048	0.027
D	0.028	0.0056	0.028	0.0056	0.022
E	0.024	0.0048	0.024	0.0048	0.020

TABLE 6. Details of the mesh resolution for the FVM cases:  $(\dots)_w$ , near the wall;  $(\dots)_c$ , near the centre of an REV-L. ‘ $\Delta x_3$ ’ was uniformly distributed.

sensitive to the fine-scale resolution, as can be seen in figure 14 comparing low- and high-resolution energy spectrum data.

Future studies should address increase of the Reynolds number beyond 1000, which was the maximum Reynolds number used in our study. The periodicity and two-dimensionality of the solid matrix used in this research should also be relaxed. Porous media with larger tortuosity could also be considered.

### Acknowledgements

The authors gratefully acknowledge the support of this study by the DFG (Deutsche Forschungsgemeinschaft) and the HLRN (North-German Supercomputing Alliance). All the parallel computations in the present study were performed at the HLRN. A.V.K. acknowledges with gratitude the support of the Alexander von Humboldt Foundation through the Humboldt Research Award.

### Appendix A

The meshes for the FVM cases are body fitted and are concentrated near the wall, while they are uniformly distributed for the LBM cases. More details, such as the ratios of the cell size  $\Delta x_i$  to the obstacle size  $d$  near the wall and near the channel centre, are given in table 6.

Two kinds of initial conditions have been tested in our study. The first one is the uniform velocity field plus a sinusoidal perturbation which has the form

$$u_i(x_j) = u_m + A_{1i} \sin(\varphi_{1i}x_j) + A_{2i} \sin(\varphi_{2i}x_j) + A_{3i} \sin(\varphi_{3i}x_j) + A_{4i} \sin(\varphi_{4i}x_j), \quad (\text{A } 1)$$

where  $u_m$  is the mean velocity shown in figure 1. Here,  $A_{ki}$  and  $\varphi_{ki}$  are parameters of an artificial perturbation. The second type of initial condition is an interpolation of the initial field from another fully developed turbulent flow. Our numerical simulations show that the statistical results of the fully developed flow field are not influenced by the initial field.

The time steps for the LBM cases are 0.000625 non-dimensional time units for  $Re = 500$  (test cases A–C) and 0.0003 non-dimensional time units for  $Re = 1000$  (test

case F). Here, the time is normalized by  $d/u_m$ . A larger time step ( $\Delta t = 0.01$ ) is used in our FVM cases since an implicit backward Euler method is employed for time marching. The test cases were computed until the statistical values, such as the turbulent two-point correlations, did not change with time any more. This process usually needs the computation of 250 wash-out cycles in one REV-L element, which is 1000 time units in case A, for example.

## REFERENCES

- AFGAN, I., KAHIL, Y., BENHAMADOUCHE, S. & SAGAUT, P. 2011 Large eddy simulation of the flow around single and two side-by-side cylinders at subcritical Reynolds numbers. *Phys. Fluids* **23**, 075101.
- AIDUN, C. K. & CLAUSEN, J. R. 2009 Lattice-Boltzmann method for complex flows. *Annu. Rev. Fluid Mech.* **41**, 439–472.
- ANTOHE, B. V. & LAGE, J. L. 1997 A general two-equation macroscopic turbulence model for incompressible flow in porous media. *Intl J. Heat Mass Transfer* **40**, 3013–3024.
- BALAKUMAR, B. J. & ADRIAN, R. J. 2007 Large- and very-large-scale motions in channel and boundary-layer flows. *Phil. Trans. R. Soc. Lond. A* **365**, 665–681.
- BHATNAGAR, P. L., GROSS, E. P. & KROOK, M. 1954 A model for collision processes in gases. I. Small amplitude processes in charged and neutral one-component systems. *Phys. Rev.* **94**, 511–525.
- DULLIEN, F. A. L. 1992 *Porous Media: Fluid Transport and Pore Structure*, 2nd edn. Academic Press.
- GUALA, M., HOMMEMA, S. E. & ADRIAN, R. J. 2006 Large-scale and very-large-scale motions in turbulent pipe flow. *J. Fluid Mech.* **554**, 521–542.
- HERWIG, H. 2002 *Strömungsmechanik*. Springer.
- JIMENEZ, J. 1998 The largest scales of turbulent wall flows. In *Center for Turbulence Research, Annual Research Briefs*, pp. 137–154. Stanford University.
- JIN, Y. & HERWIG, H. 2013 From single obstacles to wall roughness: some fundamental investigations based on DNS results for turbulent channel flow. *Z. Angew. Math. Phys.* **64**, 1337–1352.
- JIN, Y. & HERWIG, H. 2014 Turbulent flow in channels with shark skin surfaces: entropy generation and its physical significance. *Intl J. Heat Mass Transfer* **70**, 10–22.
- JIN, Y., UTH, M.-F. & HERWIG, H. 2015 Structure of a turbulent flow through plane channels with smooth and rough walls: an analysis based on high resolution DNS results. *Comput. Fluids* **107** (31), 77–88.
- KAZEROONI, R. B. & HANNANI, S. K. 2009 Simulation of turbulent flow through porous media employing a  $\nu_2f$  model. *Sci. Iran. Trans. B* **16**, 159–167.
- KIS, P. 2011 Analyse turbulenter gemischter Konvektion auf der Basis von DNS-Daten. PhD dissertation, TU Hamburg-Harburg, Verlag Dr Hut, München, ISBN 978-3-8439-0104-8.
- KOLMOGOROV, A. N. 1941 Dissipation of energy in locally isotropic turbulence. *Dokl. Akad. Nauk SSSR* **32**, 19–21.
- KUNDU, P., KUMAR, V. & MISHRA, I. M. 2014 Numerical modeling of turbulent flow through isotropic porous media. *Intl J. Heat Mass Transfer* **75**, 40–57.
- KUWAHARA, F., KAMEYAMA, Y., YAMASHITA, S. & NAKAYAMA, A. 1998 Numerical modeling of turbulent flow in porous media using a spatially periodic array. *J. Porous Media* **1**, 47–55.
- LAGE, J. L., DE LEMOS, M. J. S. & NIELD, D. A. 2002 Modeling turbulence in porous media. In *Transport Phenomena in Porous Media II* (ed. D. B. Ingham & I. Pop), pp. 198–230. Elsevier.
- LEE, K. B. & HOWELL, J. R. 1991 Theoretical and experimental heat and mass transfer in highly porous media. *Intl J. Heat Mass Transfer* **34**, 2123–2132.
- DE LEMOS, M. J. S. 2004 Turbulent heat and mass transfer in porous media. In *Emerging Technologies and Techniques in Porous Media* (ed. D. B. Ingham, A. Bejan, E. Mamut & I. Pop), pp. 157–168. Kluwer Academic.

- DE LEMOS, M. J. S. 2005 The double-decomposition concept for turbulent transport in porous media. In *Transport Phenomena in Porous Media III* (ed. D. B. Ingham & I. Pop), pp. 1–33. Elsevier.
- DE LEMOS, M. J. S. 2012 *Turbulence in Porous Media, Modeling and Applications*, 2nd edn. Elsevier.
- DE LEMOS, M. J. S. & BRAGA, E. J. 2003 Modeling of turbulent natural convection in porous media. *Intl Commun. Heat Mass Transfer* **30**, 615–624.
- DE LEMOS, M. J. S. & MESQUITA, M. S. 2003 Turbulent mass transport in saturated rigid porous media. *Heat Mass Transfer* **30**, 105–113.
- DE LEMOS, M. J. S. & PEDRAS, M. H. J. 2000 On the definitions of turbulent kinetic energy for flow in porous media. *Intl Commun. Heat Mass Transfer* **27**, 211–220.
- DE LEMOS, M. J. S. & PEDRAS, M. H. J. 2001 Recent mathematical models for turbulent flow in saturated rigid porous media. *Trans. ASME J. Fluids Engng* **123**, 935–940.
- DE LEMOS, M. J. S. & ROCAMORA, F. D. 2002 Turbulent transport modeling for heat flow in rigid porous media. In *Heat Transfer 2002, Proceedings of the 12th Intl Heat Transfer Conference*, vol. 2, pp. 791–796. Elsevier.
- DE LEMOS, M. J. S. & TOFANELI, L. A. 2004 Modelling of double-diffusive turbulent natural convection in porous media. *Intl J. Heat Mass Transfer* **47**, 4233–4241.
- MA, X., KARAMANOS, G. S. & KARNIADAKIS, G. E. 2000 Dynamics and low-dimensionality of a turbulent near wake. *J. Fluid Mech.* **410**, 29–65.
- MOIN, P. & MAHESH, K. 1998 Direct numerical simulation: a tool in turbulence research. *Annu. Rev. Fluid Mech.* **30**, 538–539.
- NAKAYAMA, A. & KUWAHARA, F. 1999 A macroscopic turbulence model for flow in a porous medium. *Trans. ASME J. Fluids Engng* **121**, 427–433.
- NIELD, D. A. 1991 The limitations of the Brinkman–Forchheimer equation in modeling flow in a saturated porous medium and at an interface. *Intl J. Heat Fluid Flow* **12**, 269–272.
- NIELD, D. A. 2001 Alternative models of turbulence in a porous medium, and related matters. *Trans. ASME J. Fluids Engng* **123**, 928–931.
- NIELD, D. A. & BEJAN, A. 1992 *Convection in Porous Media*, 1st edn. p. 8. Springer.
- NIELD, D. A. & BEJAN, A. 2013 *Convection in Porous Media*, 4th edn. Springer.
- PARNAUDEAU, P., CARLIER, J., HEITZ, D. & LAMBALLAIS, E. 2008 Experimental and numerical studies of the flow over a circular cylinder at Reynolds number 3900. *Phys. Fluids* **20**, 085101.
- PEDRAS, M. H. J. & DE LEMOS, M. J. S. 2000 On the definition of turbulent kinetic energy for flow in porous media. *Intl Commun. Heat Mass Transfer* **27**, 211–220.
- PEDRAS, M. H. J. & DE LEMOS, M. J. S. 2001a Macroscopic turbulence modeling for incompressible flow through undeformable porous media. *Intl J. Heat Mass Transfer* **44**, 1081–1093.
- PEDRAS, M. H. J. & DE LEMOS, M. J. S. 2001b Simulation of turbulent flow in porous media using a spatially periodic array and low  $Re$  two-equation closure. *Numer. Heat Transfer A* **39**, 35–59.
- PEDRAS, M. H. J. & DE LEMOS, M. J. S. 2001c On the mathematical description and simulation of turbulent flow in a porous medium formed by an array of elliptical rods. *Trans. ASME J. Fluids Engng* **123**, 941–947.
- PEDRAS, M. H. J. & DE LEMOS, M. J. S. 2003 Computation of turbulent flow in porous media using a low Reynolds number  $k$ – $\epsilon$  model and an infinite array of transversely displaced elliptic rods. *Numer. Heat Transfer A* **43**, 585–602.
- POPE, S. B. 2000 *Turbulent Flows*. Cambridge University Press.
- PRESCOTT, P. J. & INCROPERA, F. P. 1995 The effect of turbulence on solidification of a binary metal alloy with electromagnetic stirring. *Trans. ASME J. Heat Transfer* **117**, 716–724.
- ROCAMORA, F. D. & DE LEMOS, M. J. S. 2000 Analysis of convective heat transfer for turbulent flow in saturated porous media. *Intl Commun. Heat Mass Transfer* **27**, 825–834.
- SILVA, R. A. & DE LEMOS, M. J. S. 2003 Turbulent flow in a channel occupied by a porous layer considering the stress jump at the interface. *Intl J. Heat Mass Transfer* **46**, 5113–5136.
- SUCCI, S. 2001 *The Lattice Boltzmann Equation for Fluid Dynamics and Beyond*. Oxford University Press.

- VAFAI, K., MINKOWYCZ, W. J., BEJAN, A. & KHANAFER, K. 2006 Synthesis of models for turbulent transport through porous media. In *Handbook of Numerical Heat Transfer* (ed. W. J. Minkowycz & E. M. Sparrow), chap. 12, Wiley.
- WIBEL, W. & EHRHARD, P. 2006 Experiments on liquid pressure-drop in rectangular microchannels, subject to non-unity aspect ratio and finite roughness. In *Proceedings of Fourth International Conference on Nanochannels, Microchannels and Minichannels, Limerick, Ireland*.
- WIBEL, W. & EHRHARD, P. 2009 Experiments on the laminar/turbulent transition of liquid flows in rectangular microchannels. *Heat Transfer Engng* **30**, 70–77.